

1 Brief communication - Vent opening at Campi Flegrei: clues from 2 dyke propagation patterns

3 Jacopo Selva^{1,2}, Nello Mangone¹

4 ¹Dipartimento di Scienze della Terra, dell'Ambiente e delle Risorse (DiSTAR), University of Naples Federico II, Naples Italy

5 ²Istituto Nazionale di Geofisica e Vulcanologia, Osservatorio Vesuviano, Naples Italy

6 *Correspondence to:* Jacopo Selva (jacopo.selva@unina.it)

7 **Abstract.** Forecasting future vent opening position is fundamental for managing volcanic hazards, and is usually based on
8 the spatial density of past vents or other crust weakness indicators. Here, a novel empirical approach inspired by dyke
9 propagation models is applied to the Campi Flegrei caldera. Results show that dyke azimuthal direction and propagation
10 length are statistically independent, that azimuth correlates with topographic peaks within 7 km from the caldera centre, and
11 that propagation length exhibits two main peaks at 2 and 4 km. Based on these results, we develop two new vent opening
12 probability maps with maxima well correlating with caldera's structure and recent seismicity.

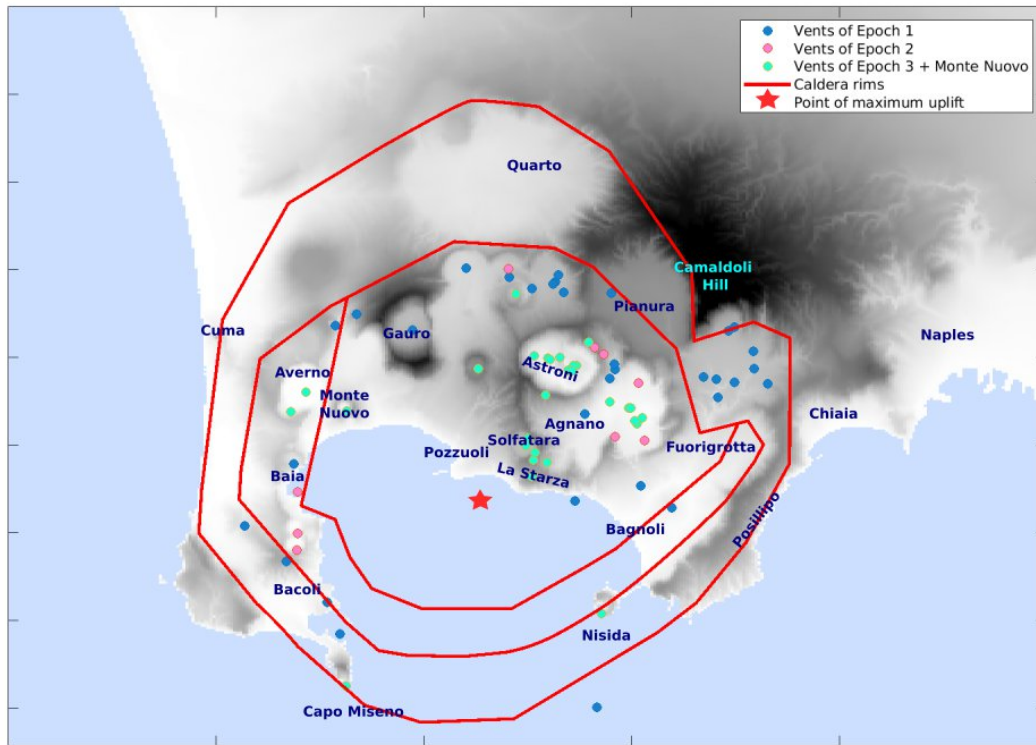
13 1 Introduction

14 The Campi Flegrei caldera volcanic activity dates back to the upper Pleistocene, with the earliest volcanic activity observed
15 in outcrops estimated at approximately 80 kyr (Pappalardo et al., 1999; Scarpati et al., 2013). Recent studies identified
16 widespread tephra layers originated from Campi Flegrei, extending its activity to nearly 200 kyr (e.g., Monaco et al., 2022;
17 Fernandez et al., 2024; Sparice et al., 2024). The first caldera collapse occurred approximately 39,000 years ago with the
18 Campanian Ignimbrite (CI) eruption (Giaccio et al., 2017). A second major eruption occurred around 14,000 years ago, the
19 Neapolitan Yellow Tuff (NYT), possibly causing a second collapse, after which volcanic activity resumed within the caldera
20 (Orsi et al., 2004).

21 The post-NYT eruptive history is divided into three main epochs (Di Vito et al., 1999, Bevilacqua et al., 2016, Fig. 1). The
22 first epoch comprises at least 33 eruptions, spanning from 14,000 to 10,600 years ago. The eruptive vents align with the
23 caldera boundaries, with the most energetic eruption being that of the "Pomici Principali" around 12,000 years ago
24 (Bevilacqua et al., 2016). The second epoch follows a relatively brief quiescent period and includes nine eruptions dated
25 between 9,600 and 9,100 years ago, primarily concentrated in the northeastern sector of the caldera. The third epoch
26 encompasses a total of 26 eruptions from approximately 5,500 to 3,800 years ago. Its activity was predominantly focused in
27 the northeastern part of the caldera (Agnano area), secondarily in the northwestern sector (Averno area), and concluded with
28 peripheral distal eruptions (Nisida, Capo Miseno, and Fossa Lupara, Natale et al., 2025). The most energetic eruption during
29 this period was that of Agnano-Monte Spina around 4,500 years ago (Bevilacqua et al., 2016). The long period of quiescence
30 following the third epoch lasted until 1538 AD, when the Monte Nuovo eruption took place in the northwestern sector of the
31 caldera (Di Vito et al., 2016). The caldera has not experienced any eruption since.

32 After NYT, the caldera experienced significant resurgence, accompanied by seismicity, degassing, and slow ground
33 deformation often referred to as bradyseism (Isaia et al., 2019; Natale et al., 2022). The latter is centred mainly in the
34 Pozzuoli area, which is approximately at the centre of the caldera (Fig. 1), and major movements were tracked at least from
35 the 4th century AD thanks to the ruins of a Roman temple in the port of this city, known as the Serapeum (Di Vito et al.,
36 2016; Vitale and Natale, 2023). The largest known bradyseismic events are the ones related to the last Campi Flegrei
37 eruption (the 1538 Monte Nuovo eruption, Di Vito et al., 2016). In the last century, three main bradyseismic crises occurred

38 in 1950-52, 1970-72, and 1982-84, characterised by episodes of uplift of almost 2 m interrupting a slow long-lasting
39 subsidence (Del Gaudio et al 2010). Approximately in 2005, a slow uplift started, accelerating over time, which fully
40 recovered the subsidence in 2021, and now exceeds the uplift peaks observed in the last century (Bevilacqua et al., 2024).
41 This event is still ongoing.



42
43 **Figure 1:** Topographic map of the Campi Flegrei caldera, along with the vent positions of post-NYT eruptions (from Bevilacqua et al.,
44 2016) and the caldera rims active in the last 40 ka (Natale et al., 2024, 2025). For simplicity, Monte Nuovo is included in Epoch 3. Darker
45 colours mean higher elevations.

46
47
48 Forecasting vent opening is crucial for any volcanic hazard quantification. Different approaches were adopted at Campi
49 Flegrei through time. Alberico et al., (2002) developed a method identifying crustal weaknesses using geophysical,
50 geological, and geochemical parameters. Their probability map indicates the highest likelihood of vent openings in the
51 central caldera near Pozzuoli (Fig. 1). Selva et al., (2012) utilized a Bayesian approach fed by fewer parameters, focusing on
52 tectonic structures recognized at that time, to track crust weakness, and past vents, shifting the area at higher probability
53 toward the northeastern and northwestern sectors, where post-NYT activity concentrated. Bevilacqua et al., (2015) adopted a
54 method based on Gaussian kernel and accounting for the uncertainty on past vent positions, confirming the northeastern
55 sector (near Agnano and Astroni, Fig. 1) as the most likely area for future eruptions. Both Selva et al., (2012) and Bevilacqua
56 et al., (2015) included also a formal quantification of the epistemic uncertainty in their models, accounting for model
57 uncertainty. More recently, based on past observations and removing multiple eruptions from clustered vents, Charlton et al.,
58 (2020) noted that vent opening occurred substantially randomly within a ring area surrounding the caldera centre,
59 corresponding to the caldera rim (Fig. 1), producing a new qualitative indication about potential future vent opening.

60 Rivalta et al., (2019) studied the physical propagation of magma dykes by modelling the trajectory of potential dykes due to
 61 the subsurface stress field and the dike's initial position. Their model accounts for various stresses affecting magma ascent.
 62 For calderas, it suggests that eruptive vents are concentrated at specific distances from the centre, influenced by the stress
 63 induced by the caldera depression, defining a higher propensity to eruption closer to caldera rims, as noted by Charlton et al.,
 64 (2020). Considering the caldera depression size, Rivalta et al., (2019) forecasted for Campi Flegrei a potential peak for vent
 65 opening at a semi-annular belt located between 2.3 and 4.2 km from the caldera centre. Rivalta et al., (2019) analysed also
 66 the effect of caldera unloading, as well as those of topographic peaks, which may break the caldera symmetry. They analysed
 67 the case of the Campi Flegrei caldera, explaining the concentration of volcanic activity in the northeastern sector due to the
 68 topographic peak of the Camaldoli Hill (Fig. 1), which creates a stress field that may favour magma trajectories in the north-
 69 east direction.

70 The main features of Rivalta et al., (2019) model are i) that the geometry of the caldera (unloading effect) significantly
 71 influences dykes propagation outward, promoting eruptions away from the geometric centre of the caldera, and ii)
 72 topographic asymmetries create localised stress variations in the subsurface, affecting eruption frequency across different
 73 angular sectors. While a sufficiently detailed knowledge of the sub-surface stress state is difficult to reach, it is possible to
 74 verify if these two main features left a trace on the available record of past vent positions, and to use this empirical signature
 75 to define new vent opening probability maps.

76 2 Method

77 Rivalta et al., (2019) found that the path of the dykes feeding eruptions is mainly controlled by the geometry of the caldera,
 78 which determines the distance from the centre of the caldera, and by the topographic peaks surrounding the caldera, which
 79 establishes preferential directions for propagation. To this end, for Campi Flegrei Rivalta et al., (2019) assumed that the
 80 origin at depth of the magma is located at the centre of the caldera, 3 km below the location of the maximum observed uplift
 81 (Amoruso et al., 2014a, Rivalta et al., 2019, Buono et al., 2025), and producing mostly lateral propagation with trajectories
 82 controlled by the structure of the caldera and the consequent stress distribution within the caldera. In other words, Rivalta et
 83 al. (2019) demonstrate that, in an approximately symmetric caldera with a given magma source located around the centre of
 84 the caldera, independently of its specific depth and size, we expect a symmetrical radial dyke propagation from the source,
 85 and with preferred directions controlled by local factors. The empirical track of these features may be retrieved by studying
 86 the distribution of past vents around the caldera centre, being this position not necessarily the origin point for dykes, which
 87 may indeed detach from the edge of the source (Gregg et al. 2012; Rivalta et al. 2019), but simply the reference for tracking
 88 the radial symmetry.

89 Assuming a similar magma origin also for future eruptions, these empirical distributions can then be used to set a vent
 90 opening probability map. The probability density function in a specific point in the caldera can be calculated in polar
 91 coordinates using the following formula:

$$92 \quad f_{pol}(r,\theta) = f_r(r)f_\theta(\theta). \quad (1)$$

93 where the term $f_r(r)$ is the probability distribution for the distances from the centre of the caldera, and the term $f_\theta(\theta)$ is the
 94 angular probability distribution. In this formulation, it is assumed that these two distributions can be considered independent.
 95 Indeed, the physical process described in Rivalta et al., (2019) suggests a potential independence between direction of dyke
 96 propagation and distance from the caldera centre, as they are controlled by two different features of the caldera, being the
 97 distance fundamentally controlled by the size of the nearly circular shape of the caldera, and the direction predominantly
 98 controlled by local topographic features. This independence should also leave an empirical track in past vent positions,
 99 which can also be formally verified by testing whether the direction and the distances found using past vent positions are
 100 correlated to each other.

101 The probability distribution of eq. (1) can be transformed into Cartesian coordinates as follows:

$$102 \quad f_{xy}(x,y) = \frac{1}{r} f_{pol}(r,\theta) = \frac{1}{r} f_r(r)f_\theta(\theta) \quad . \quad (2)$$

103 where the term $f_{pol}(r,\theta)$ is again factorized in its two terms using Eq. (1). Defining an application grid, equation (2) can be
 104 used to establish a vent probability map by substituting $f_r(r)$ and $f_\theta(\theta)$ with the appropriate distributions of potential distance-

105 from-centre and azimuth. Depending on the available data, such distributions may be estimated empirically, looking at the
106 distribution of past vents, including all the data that reflect the present state of the caldera, or analysing the topographical
107 peaks surrounding the caldera.

108 3. Results

109 At Campi Flegrei, an oblate central pressurized melt zone located at the center of the caldera is compatible with many
110 geophysical evidences (e.g. Barberi et al., 1991; Capuano et al. 2013; Castaldo et al. 2021; De Leandro et al. 2025). Inflation
111 of a caldera-centered oblate spheroidal magma chamber at a depth of ~ 3.5 km is consistent with the deformation in the last
112 ~ 600 years at least (Di Vito et al. 2016, D’Auria et al. 2015, Amoruso et al. 2007, 2014b), and a similar source is likely
113 active at least in the last 5 ka (Di Vito et al. 2016; Rivalta et al. 2019). The position of the caldera centre is here assumed at
114 the point of maximum uplift, here set 800 meters south of the GNSS station of Rite at coordinates Easting 426355 and
115 Northing 4518743 (UTM WGS84, zone 33N; Bevilacqua et al., 2024, Fig. 1). To establish an empirical model, we study the
116 empirical distribution of azimuth (angle to the North of the line connecting the centre of the caldera and the vent, hereinafter
117 azimuth) and of the distance from the centre of the caldera (hereinafter distance) of past eruptions. We consider the 71 vent
118 positions of the post-NYT activity (Bevilacqua et al., 2016). The stability of these empirical distributions on the specific
119 location of the caldera center is tested by sampling other possible centers in boxes of 1 and 2 km around the selected centre
120 (Supplementary Figure 1). Past vent positions are also affected by significant uncertainty. To evaluate their potential impact
121 on all statistical analyses, we consider the uncertainty bounds defined in Bevilacqua et al., (2016), accounting for the
122 uncertainty by randomly sampling 1000 alternative synthetic positions uniformly distributed within the defined uncertainty
123 bounds (Supplementary Figure 1).

124 3.1 Empirical distributions of distance and azimuth

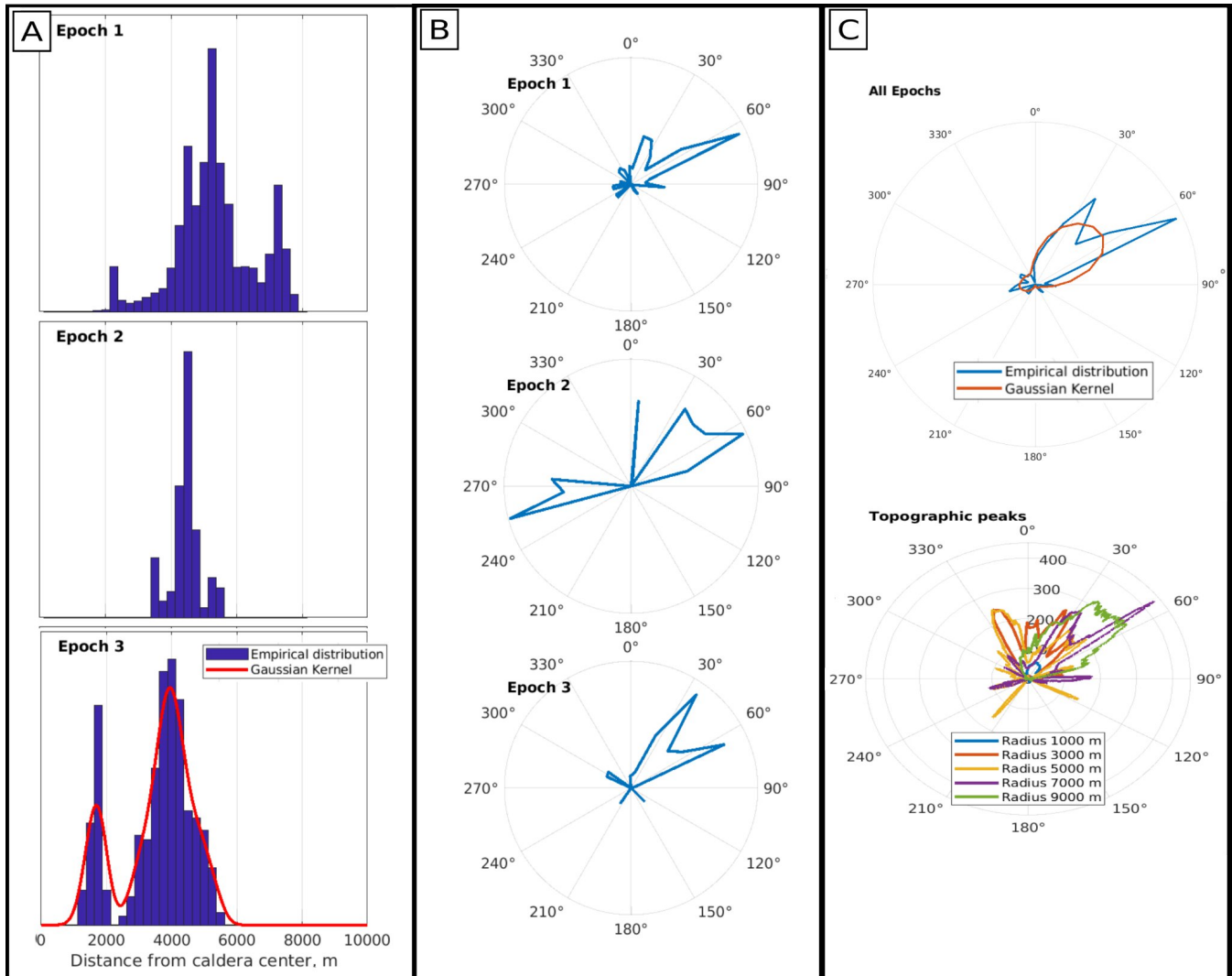
125 We first analyse the distances between the centre of the caldera and all post-NYT vents. The analysis is conducted separately
126 for the three epochs. For simplicity, the recent Monte Nuovo eruption is included in the third epoch. In Figure 2A, we report
127 the empirical distributions (histograms with bins of 250 m, the corresponding empirical cumulative distributions are reported
128 in Supplementary Figure 2), revealing a strong difference between the first epoch, where 60% of eruptions occur between
129 4,400 and 6,600 m, and the third epoch that shows shorter distances, with two significant peaks around 4,000 m and 2,000 m,
130 being Epoch 2 somehow intermediate between the other two. The results are stable for different selected centers of the
131 caldera (Supplementary Figure 3).

132 To test if the distributions for the different Epochs are different, we implement a two-sample Kolmogorov-Smirnov test
133 (KS2), a non-parametric statistical test used to determine if two independent datasets are drawn from the same underlying
134 distribution (Gibbons and Chakraborti, 2003). Here and in the following tests, the significance level (red line in figures) is
135 set to 0.01 and it is corrected for multiple testing using the Bonferroni (1936) criterion, which consists of dividing the
136 significance level by the number of comparisons. The test confirms that the difference between Epoch 1 and Epoch 3 is
137 statistically significant also accounting for vent position uncertainty (see Supplementary Figure 4), confirming the already
138 observed progressive inward migration of post-NYT volcanism (Rivalta et al., 2019).

139 Following Rivalta et al., (2019), the direction of propagation of the dykes is controlled by topographic asymmetries. This
140 direction can be investigated by analysing the azimuth of past vents with respect to the centre of the caldera. In Figure 2B,
141 we report the empirical distributions for the different epochs (histogram with bins of 20 degrees, the corresponding empirical
142 cumulative distribution functions are reported in Supplementary Figure 2), showing that most of eruptions have an azimuth
143 toward NE (50° , toward Astroni, Agnano, and Solfatara). Also in this case, the results are stable for different selected centers
144 of the caldera (Supplementary Figure 3). No specific differences between the distributions are visible. This observation is
145 tested again with a two-sample Kolmogorov-Smirnov test (see Supplementary Figure 4), confirming that the directions of
146 dyke propagation are similar in all epochs.

147 Rivalta et al., (2019) suggest that preferential directions may be induced by topographic peaks that locally modify the stress
148 field, which is mainly controlled by unloading. To investigate this empirically, we analyse the maxima of the topography
149 surrounding the caldera, retrieving the maxima in all directions in swaths with different length, hereinafter called radius.
150

152 Maximum radii from 1 to 9 km are tested: for each radius, the distribution of topographic maxima as a function of azimuth is
 153 normalised and compared with the azimuthal distribution of past eruptions (Figure 2C). For simplicity, the present day
 154 topography is adopted, even if some of the edifices (and the corresponding topographic peaks) were built throughout the
 155 post-NYT activity. The comparison confirms the correlation anticipated by Rivalta et al., (2019). The primary peak is NE
 156 (around 50°) corresponds to the topographic peak associated with Accademia and La Pietra area (Fig. 1, for a radius of 1 km)
 157 and Camaldoli Hill (for radii of 3 km and larger). In agreement with Rivalta et al., (2019), the latter topographic peak is the
 158 most pronounced and it coincides with the highest concentration of eruptive vents during various eruptive periods. A
 159 secondary peak appears in the NNW direction (around 330°) for intermediate radii (between 3 and 5 km), corresponding to
 160 the peak of the Gauro volcanic edifice (Monte Barbaro): this edifice was created during one of the first eruptions of the first
 161 epoch, and does not correspond to any peak in the observed distribution of azimuth. However, this secondary peak becomes
 162 less important for large radii (7 km and above), due to the prevalence of the Camaldoli Hill. Performing a Kolmogorov-
 163 Smirnov test between the angular distributions of past vents and of topographic peaks, the largest p-values correspond to a
 164 maximum distance of 7 km. The null hypothesis of equal distribution is consistently not rejected independently from vent
 165 position uncertainty only for radii of 7 and 9 km, while it is rejected for smaller radii (Supplementary Figure 5).
 166



167

168 **Figure 2:** (A) Empirical distribution of distances from the centre of the caldera (dyke propagation length) for Epochs 1, 2 and 3. The red
169 line in Epoch 3 reports a Gaussian kernel smoothing the empirical distribution. (B) Empirical distribution of azimuth (dyke direction) for
170 Epochs 1, 2 and 3. (C) Empirical distribution of azimuth (dyke direction) for all Epochs (the red line in Epoch 3 reports a Gaussian kernel
171 smoothing the empirical distribution) and the maxima of topographic peaks in radial swaths of variable length from the caldera centre.

172 3.2 Vent opening probability for Campi Flegrei

173 To apply Eq. (2) and quantify the vent probability map, we first test the independence of the radial and the azimuth
174 distributions, by testing whether the direction and the distances of past vent positions are correlated to each other. To this
175 end, we divide the directions in the 4 sectors (SW, NW, NE, and SE), and we compare the distribution of distances in the
176 different sectors again using the Kolmogorov-Smirnov test. All the six couples are tested. The results (see Supplementary
177 Figure 6) show that the hypothesis of equal distribution cannot be rejected for all combinations of sectors. This means that
178 the distribution of distances in the different directions (with different azimuth) are statistically equal, standing for the
179 independence between distance and azimuth.

180 To develop the probability map, we define a grid 14.5 x 12.5 km, centred at Easting 427406 and Northing 4518958 (UTM
181 WGS 84 33N), with 700 square cells 500 x 500 m, equal to the one adopted in Selva et al., (2012). Then, the probability in
182 each cell is computed by numerically integrating $f_{xy}(x,y)$ computed through Eq. (2), where the terms $f_r(r)$ and $f_\theta(\theta)$ can be
183 set using the empirical distributions developed in Section 3.1.

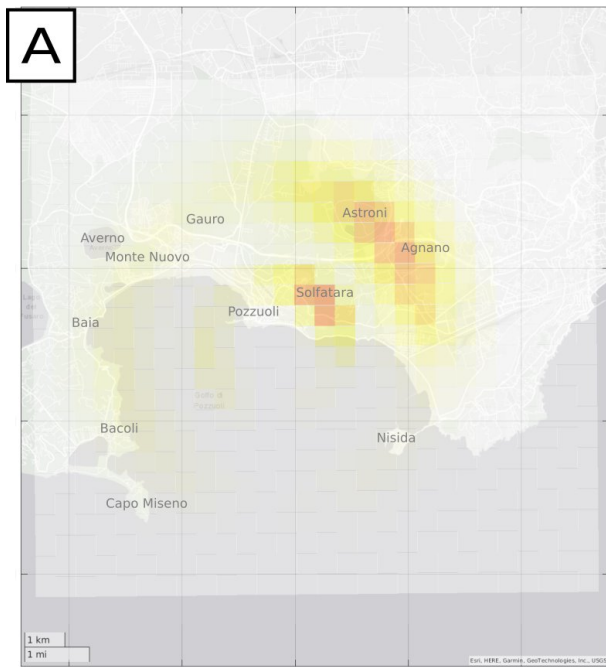
184 In particular, we propose 2 alternative implementations. At first, we consider for both $f_r(r)$ and $f_\theta(\theta)$ the empirical
185 distributions that may be considered representatives of the present state of the caldera. Hereinafter, this first approach is
186 referred to as model M1. To generalize the empirical distributions, we apply Gaussian kernels (red curves in Fig. 2A,C). The
187 most appropriate bandwidth is defined using a leave-one-out technique with a Kullback-Leiber score (Connor et al., 2019).
188 We set $f_r(r)$ as the radial distribution of the eruptions of Epoch 3 only (including also Monte Nuovo), i.e. the most recent. As
189 Epoch 1 is significantly different for the distribution of distances, its consideration would introduce a bias for forecasting
190 future behaviours. Here, being very close in time to Epoch 1, Epoch 2 is assimilated to it, and only Epoch 3 is considered.
191 The distribution is also truncated at 10 km, where it essentially drops to 0 (red line in Fig. 1A). The more appropriate
192 bandwidth is found to be 275 m (Supplementary Figure 7a). To set $f_\theta(\theta)$, we instead consider the azimuth distribution of all
193 post-NYT eruptions (red line in Fig 1C), as the different epochs are statistically indistinguishable. For the kernel, the more
194 appropriate bandwidth is found to be 17 degrees (Supplementary Figure 7b).

195 A second implementation is also tested by setting $f_\theta(\theta)$ differently, that is by substituting the empirical azimuth distribution
196 adopted in M1 with the distribution of the topographic maxima for a radius of 7,000 m, the one that better correlates with
197 past vents. Hereinafter, this second approach is referred to as model M2.

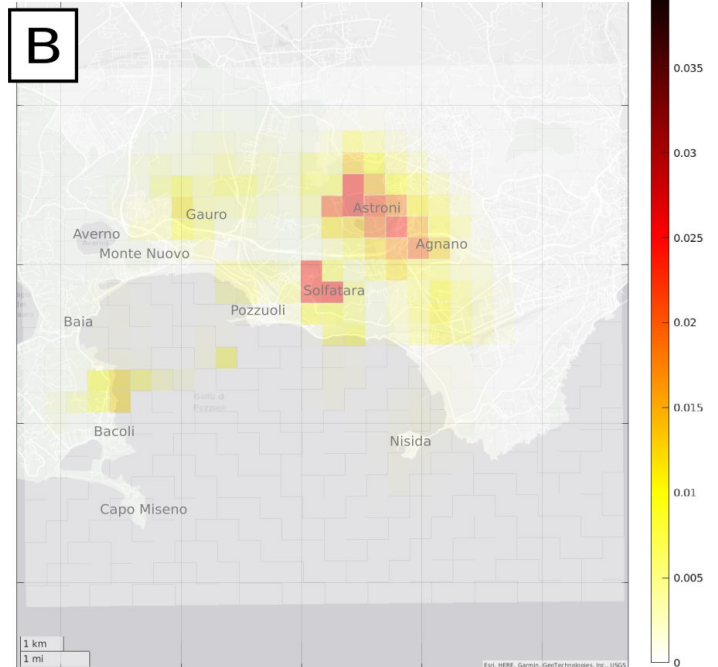
198 The results of the two alternative implementations M1 and M2 are reported in Figure 3. The numerical values for both
199 models are reported as Supplementary File. The resulting maps are similar, with two distinct probability peaks in the NE
200 direction at about 4 and 2 km from the centre, corresponding to the Agnano-Astroni and the Solfatara area, respectively. In
201 M2, which considers the topographic contribution (Figure 3B), the angular probability values are less smoothed than in
202 model M1, where the empirical distributions are smoothed by the kernels (Figure 3A). The effect is that the maximum
203 probability values in the area at NE is almost halved in M1; also the relative peaks in the other directions appear relatively
204 more evident in M2, with secondary peaks in the submerged side of the caldera toward W, in the direction of Bacoli, as well
205 as the inland area toward NNW. On the contrary, in M1 probabilities are more distributed, generating two concentric and
206 separated rings of larger probabilities at 2 and 4 km from the caldera centre.

207

M1: Empirical distributions



M2: Empirical distribution+ topographic profile



208
209
210

Figure 3: Vent opening probability maps: (A) model M1, based empirical distances and azimuth, (B) model M2, based on empirical distances and topographic azimuth.

211

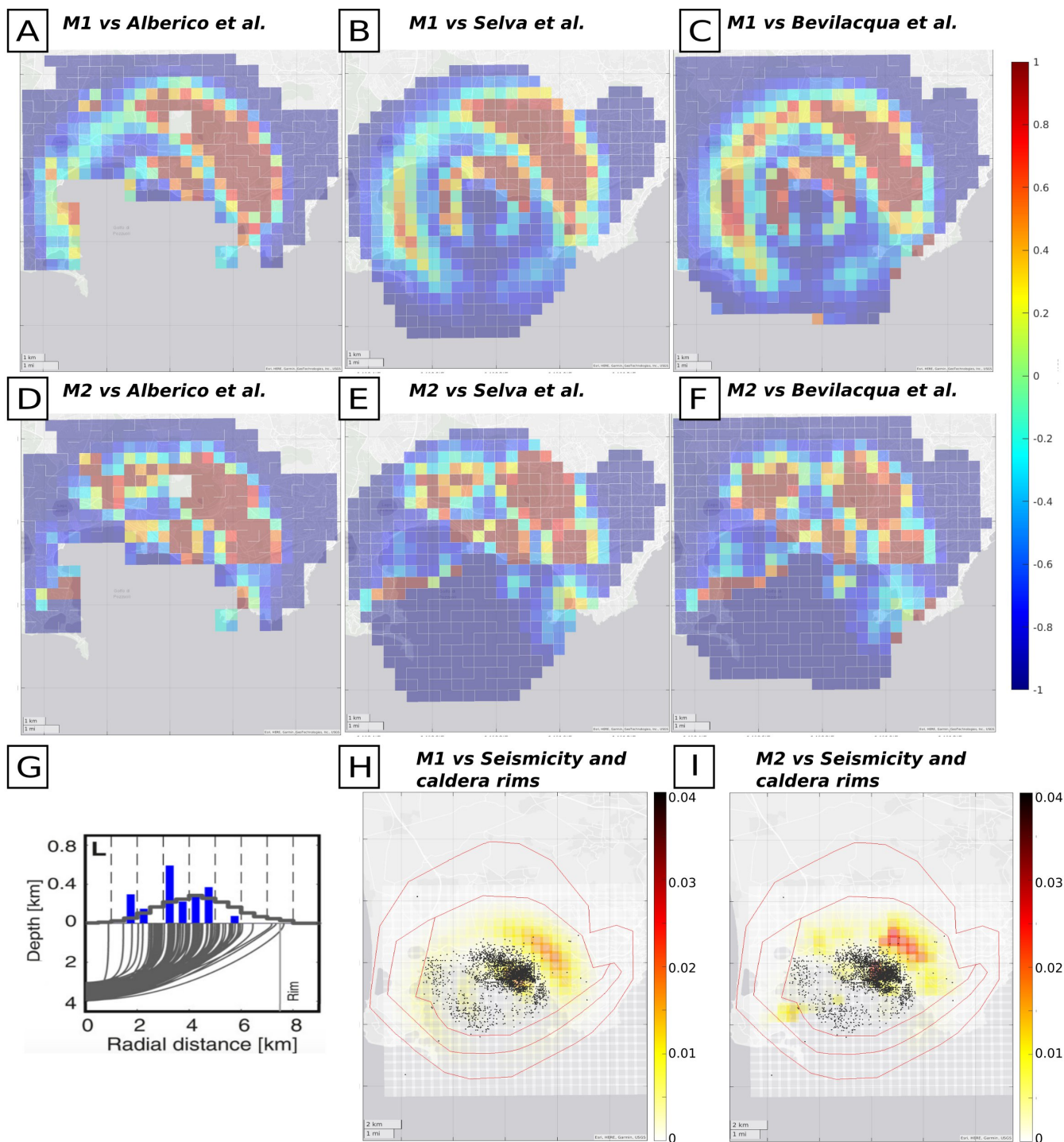
212 **4. Discussion**

213 Comparing these results with the main probability maps for Campi Flegrei discussed in the literature - Alberico et al.,
214 (2002), Selva et al., (2012), and Bevilacqua et al., (2015), hereinafter indicated as A02, S12 and B15, respectively -
215 interesting coincidences and some significant differences emerge. As already noted, the map produced by A02 differs widely
216 from S12 and B15 maps, having maximum values in the centre of the caldera, which is in contrast with the empirical
217 evidence of recent past vents. In this, M1 and M2 are closer to S12 and B15, providing lower probabilities close to the
218 caldera centre and larger probabilities in the NE area of Astroni and Agnano, where most of past vents concentrate.
219 To better highlight further similarities and differences, in Figure 4A-F we report the maps of the relative differences in
220 probability between M1, M2 and A02, S12, and B15, rescaling all of them to the same grid and, for S12 and B15,
221 considering the mean of the epistemic uncertainty (Supplementary Figure 8). These maps highlight that the main differences
222 are connected to the two ring regions with relatively higher probability discussed above, which were not present in previous
223 studies.

224 The outer ring of relatively high probability, at 4 km, which coincides with the area identified by Charlton et al., (2020),
225 includes the highest probability area of S12 and B15, located in the Agnano area to the NE of the caldera. However, also in
226 this area, both M1 and M2 provide larger probabilities (Fig. 4, panels B, C, E, F). This ring also includes the area of Monte
227 Nuovo (toward N, last eruption at Campi Flegrei), and especially M1 provides larger probabilities than previous studies.
228 Also the secondary peak identified in the Averno area (toward NW) in S12 is found in both M1 and M2, but shifted inward
229 and eastward, in the direction of Gauro. The outer ring also generates several other secondary probability peaks at sea in the
230 W direction, in the direction of the topographic peaks of Baia/Bacoli, especially in M1. These peaks are larger than in
231 literature maps. On the other hand, in the areas of Nisida (toward SE) and Capo Miseno (toward SW), the probability values
232 obtained here are relatively lower than the ones in the maps published in literature.

233 The inner ring of relatively high probability includes the high probability area of Solfatara, present in both S12 and B15, but
234 also in this case both M1 and M2 provide larger probabilities (Fig. 4B, C, E, F). In addition, the inner ring introduces new
235 peaks in probability within the bay, toward W, and in the coastal area of Accademia and La Pietra, toward E, both less
236 pronounced in previous studies.

237 Also in the outer area of the caldera, external to the outer ring of relatively high probability, M1 and M2 are different than
238 previous studies. Here, M1 and M2 do not assume that vent opening may occur only inside the caldera border, as in S12 and
239 B15, but an outer limit is established only by the maximum observed distance from the centre of the caldera in Epoch 3,
240 which is used to truncated the empirical distribution (Section 3.1). This cuts out the most external areas, mainly toward E,
241 NW and S, where both M1 and M2 foresee smaller probabilities than previous models.



242
 243 **Figure 4:** Relative difference between (A) M1 and Alberico et al., (2002), (B) M2 and Alberico et al., (2002), (C) M1 and Selva et al.,
 244 (2012), (D) M2 and Selva et al., (2012), (E) M1 and Bevilacqua et al., (2015), (F) M2 and Bevilacqua et al., (2015). Relative differences
 245 are computed as the difference between our model (M1 or M2) and the literature model, divided by the literature model. Positive/negative
 246 numbers mean that M1/M2 are larger/smaller than literature studies, and a value equal to 1 means 100% over-estimation (double) or

247 larger. (G) Forecasted distances from the centre of the caldera from Rivalta et al., (2019) for dyke propagation compared with observed
248 vent radii (blue bars). (H-I) Comparison between the spatial distribution of Campi Flegrei seismicity ($M_d > 0.5$) in the period June 2023 -
249 June 2025, the caldera rims (as mapped in Natale et al., 2024, 2025), and M1 (panel H) and M2 (panel I).

250 251 **5. Conclusions**

252 The vent opening maps derived in the study are based on assumptions radically different from the ones in literature. The
253 approach is inspired from the dyke propagation model proposed in Rivalta et al., (2019), which suggests a substantial
254 independence between the radial and azimuthal distributions of dykes propagating from a finite source located at the centre
255 of the caldera. The results confirm some of the features already highlighted in previous studies, but also it introduces
256 important differences. In particular, the most striking difference is that the vent probability peaks in two circles at around 2
257 and 4 km from the caldera centre, with significant modulations in the different directions, while smaller probabilities are
258 found in the peripheral areas of the caldera. These rings of relatively higher probability, particularly evident in model M1 but
259 present also in model M2, are compatible with in the range forecasted by Rivalta et al., (2019) when adopting only Epoch 3
260 data (Fig. 4G). However, the propagation distance distribution here produces two distinct peaks at 2 and 4 km, more than a
261 continuous distribution in this range. The inner circle essentially coincides with an area characterized by high seismic
262 activity recorded in the ongoing unrest episode (black dots in Fig. 4H,I), while the outer circle is instead closer to the
263 position of the ring faults surrounding the inner caldera (red lines in Fig. 4H-I, Natale et al., 2024, 2025). These observations
264 are completely independent and seem to spot privileged paths for magma ascent around the inner caldera border. This may
265 be the subject of future studies.

266 It is important to stress that M1 and M2 are produced using the empirical distributions which are considered relevant for
267 forecasting future occurrences, that is Epoch 3 for distances, and either all epochs or topographic peaks for azimuth. Indeed,
268 while the distribution of the azimuth does not change significantly across epochs, the analysis of the distances with respect to
269 the centre of the caldera has shown that Epoch 1 differs significantly from Epoch 3 in terms of distances. This may be sign of
270 a change in the volcanic source and/or in the active stress field, in agreement with the findings of Rivalta et al., (2019), and
271 with Orsi et al., (2004), who concluded that the last change in stress regime occurred prior to onset of the Epoch 3, and
272 suggested that only the past 5 ka should be considered as reference for the present state of the caldera (Orsi et al., 2009). This
273 assumption was adopted also in Selva et al., (2012).

274 Regarding the azimuth distribution, we found that the correlation between azimuth and topographic peaks is instead stable
275 across epochs and is maximized considering the topographic peaks within 7 km from the caldera centre, demonstrating that
276 the topography surrounding the caldera may be a good proxy for vent forecasting. In the future, this relationship may be
277 better explored at different scales in space and time, studying for example the potential effects of the varying spatio-temporal
278 morphology due to eruption history, or the impact of different positions of the magma source.

279 Finally, even if we develop two maps, we prefer not to quantify the epistemic uncertainty on the proposed approach,
280 differently from what was done in previous studies like Selva et al., (2012) and Bevilacqua et al (2015). The reason is that
281 several case studies recently demonstrated that the effective epistemic uncertainty on a target physical process (here vent
282 opening) is better estimated by combining radically alternative approaches (e.g., defining weighted ensembles of alternative
283 models), rather than by exploring the epistemic uncertainty inherent to one specific approach (Selva et al., 2018; Marzocchi
284 et al., 2021; Meletti et al., 2021, among the others). Consequently, while the epistemic uncertainty on a given approach may
285 be of relative interest, the very development of an alternative approach like the one presented here may be a significant
286 added value to future quantification of epistemic uncertainty in the process of vent opening at Campi Flegrei, via multi-
287 model ensembles or equivalent approaches that combine all the scientifically grounded approaches available in literature
288 (e.g. SSHAC 1997, Marzocchi et al., 2017, 2021).

289 290 **Code/Data availability**

291 The position of the vents related to past eruptions was obtained from Bevilacqua et al., (2015). The DEM used to find
292 topographic peaks around Campi Flegrei is TINITALY (Tarquini et al., 2023) with WGS 84 / UTM zone 33N coordinates,
293 available at <https://tinitaly.pi.ingv.it/>.

294

295 **Author contributions**

296 JS and NM conceived and developed the Methodology. JS supervised the project. NM implemented the preliminary software
297 for the analyses, with the support of JS. JS finalized the software and prepared the original draft. All the authors reviewed
298 and approved the manuscript.

299

300 **Competing interests**

301 Authors declare no competing interest.

302

303 **Acknowledgments**

304 The figures and maps have been produced using Matlab and/or InkScape software.

305

References

- 306 Alberico, I., Lirer, L., Petrosino, P., & Scandone, R. (2002). A methodology for the evaluation of long-term volcanic risk
307 from pyroclastic flows in Campi Flegrei (Italy). *Journal of Volcanology and Geothermal Research*, 116, 63–78.
308 [https://doi.org/10.1016/S0377-0273\(02\)00211-1](https://doi.org/10.1016/S0377-0273(02)00211-1)
309
- 310 Amoruso, A., Crescentini, L., Linde, A. T., Sacks, I. S., Scarpa, R., & Romano, P. (2007). A horizontal crack in a layered
311 structure satisfies deformation for the 2004–2006 uplift of Campi Flegrei. *Geophysical Research Letters*, 34, L22313.
312 <https://doi.org/10.1029/2007GL031644>
313
- 314 Amoruso, A., Crescentini, L., Sabbetta, I., De Martino, P., Obrizzo, F., & Tammaro, U. (2014a). Clues to the cause of the
315 2011–2013 Campi Flegrei caldera unrest, Italy, from continuous GPS data. *Geophysical Research Letters*, 41, 1–7.
316 <https://doi.org/10.1002/2014GL059539>
317
- 318 Amoruso, A., Crescentini, L., & Sabbetta, I. (2014b). Paired deformation sources of the Campi Flegrei caldera (Italy)
319 required by recent (1980–2010) deformation history. *Journal of Geophysical Research: Solid Earth*, 119, 858–879.
320 <https://doi.org/10.1002/2013JB010392>
321
- 322
- 323 Barberi, F., Cassano, E., La Torre, P., Sbrana, A. (1991) Structural evolution of Campi Flegrei caldera in light of
324 volcanological and geophysical data. *Journal of Volcanology and Geothermal Research* 48, 33–49,
325 [https://doi.org/10.1016/0377-0273\(91\)90031-T](https://doi.org/10.1016/0377-0273(91)90031-T)
326
- 327 Bevilacqua, A., Isaia, R., Neri, A., Vitale, S., Aspinali, W. P., Bisson, M., Flandoli, F., Baxter, P. J., Bertagnini, A., Ongaro,
328 T. E., Iannuzzi, E., Pistolesi, M., & Rosi, M. (2015). Quantifying volcanic hazard at Campi Flegrei caldera (Italy) with
329 uncertainty assessment: 1. Vent opening maps. *Journal of Geophysical Research: Solid Earth*, 120, 2309–2329.
330 <https://doi.org/10.1002/2014JB011775>
331
- 332 Bevilacqua A, Flandoli F, Neri A, Isaia R, Vitale S (2016). Temporal models for the episodic volcanism of Campi Flegrei
333 caldera (Italy) with uncertainty quantification. *J Geophys Res Solid Earth* 121:7821–7845.
334 <https://doi.org/10.1002/2016JB013171>
335
- 336 Bevilacqua, A., Neri, A., De Martino, P. et al., (2024) Accelerating upper crustal deformation and seismicity of Campi
337 Flegrei caldera (Italy), during the 2000–2023 unrest. *Commun Earth Environ* 5, 742.
338 <https://doi.org/10.1038/s43247-024-01865-y>
339

340 Bonferroni C., 1936. Teoria statistica delle classi e calcolo delle probabilità. Pubblicazioni del Regio Istituto Superiore di
341 Scienze Economiche e Commerciali di Firenze, 8, 3–62. (in Italian).
342

343 Buono, G., Maccaferri, F., Pappalardo, L., Tramelli, A., Caliro, S., Chiodini, S., Pinel, V., Rivalta, E., Spagnuolo, E.,
344 Trasatti, E., Di Vito, M.A. (2025). Weak Crust Owing Past Magmatic Intrusions Beneath Campi Flegrei Identified: The
345 Engine for Bradyseismic Movements? *AGU Advances*, 6, e2024AV001611. <https://doi.org/10.1029/2024AV001611> \

346
347 Capuano, P., Russo, G., Civetta, L., Orsi, G., D'Antonio, M., Moretti, R. (2013). The active portion of the Campi Flegrei
348 caldera structure imaged by 3-D inversion of gravity data. *Geochemistry, Geophysics, Geosystems*, 14, 4681–4697.
349 <https://doi.org/10.1002/ggge.20276>
350

351 Castaldo, R., Tizzani, P., Solaro, G. (2021). Inflating Source Imaging and Stress/Strain Field Analysis at Campi Flegrei
352 Caldera: The 2009–2013 Unrest Episode. *Remote Sensing*, 13, 2298. <https://doi.org/10.3390/rs13122298>
353

354 Charlton, D., Kilburn, C., & Edwards, S. (2020). Volcanic unrest scenarios and impact assessment at Campi Flegrei caldera,
355 Southern Italy. *Journal of Applied Volcanology*, 9(7). <https://doi.org/10.1186/s13617-020-00097-x>
356

357 Connor, C. B., L. J. Connor, A. Germa, J. A. Richardson, M. Bebbington, E. Gallant, and J. A. Saballos (2019) How to use
358 kernel density estimation as a diagnostic and forecasting tool for distributed volcanic vents, *Statistics in Volcanology* 4.3 : 1
359 – 25. <http://dx.doi.org/10.5038/2163-338X.4.3>
360

361 D'Auria, L., Massa, B., Cristiano, E., Del Gaudio, C., Giudicepietro, F., Ricciardi, G., Ricco, C. (2015) Retrieving the stress
362 field within the Campi Flegrei caldera (Southern Italy) through an integrated geodetical and seismological approach. *Pure*
363 *Appl. Geophys.* 172, 3247–3263. <https://doi.org/10.1007/s00024-014-1004-7>
364 Del Gaudio, C., Aquino, I., Ricciardi, G. P., Ricco, C., & Scandone, R. (2010). Unrest episodes at Campi Flegrei: A
365 reconstruction of vertical ground movements during 1905–2009. *Journal of Volcanology and Geothermal Research*, 195,
366 48–56. <https://doi.org/10.1016/j.jvolgeores.2010.05.014>
367

368 De Landro, G., Vanorio, T., Muzellec, T., Russo, G., Lomax, A., Virieux, J., & Zollo, A. (2025). 3D structure and dynamics
369 of Campi Flegrei enhance multi-hazard assessment. *Nature Communications*, 16, 4814. [https://doi.org/10.1038/s41467-025-](https://doi.org/10.1038/s41467-025-59821-z)
370 [59821-z](https://doi.org/10.1038/s41467-025-59821-z)
371

372 Di Vito, M. A., Acocella, V., Aiello, G., Barra, D., Battaglia, M., Carandente, A., Del Gaudio, C., De Vita, S., Ricciardi, G.
373 P., Ricco, C., Scandone, R., & Terrasi, F. (2016). Magma transfer at Campi Flegrei caldera (Italy) before the 1538 AD
374 eruption. *Scientific Reports*, 6, 32245. <https://doi.org/10.1038/srep32245>
375

376 Di Vito, M. A., Isaia, R., Orsi, G., Southon, J., de Vita, S., D'Antonio, M., Pappalardo, L., & Piochi, M. (1999). Volcanism
377 and deformation since 12,000 years at the Campi Flegrei caldera (Italy). *Journal of Volcanology and Geothermal Research*,
378 91(2–4), 221–246. [https://doi.org/10.1016/S0377-0273\(99\)00037-2](https://doi.org/10.1016/S0377-0273(99)00037-2)
379

380 Fernandez, G., Giaccio, B., Costa, A., Monaco, L., Nomade, S., Albert, P. G., Pereira, A., Flynn, M., Leicher, N., Lucchi, F.,
381 Petrosino, P., Palladino, D. M., Milia, A., Insinga, D. D., Wulf, S., Kearney, R., Veres, D., Jordanova, D., Putignano, M. L.,
382 Isaia, R., & Sottili, G. (2024). New constraints on the Middle–Late Pleistocene Campi Flegrei explosive activity and
383 Mediterranean tephrostratigraphy (~160 ka and 110–90 ka). *Quaternary Science Reviews*, 331, Article 108623.
384 <https://doi.org/10.1016/j.quascirev.2024.108623>
385

386 Giaccio, B., Hajdas, I., Isaia, R., Deino, A., Nomade, S. (2017). High-precision ^{14}C and $^{40}\text{Ar}/^{39}\text{Ar}$ dating of the Campanian
387 Ignimbrite (Y-5) reconciles the time-scales of climatic-cultural processes at 40 ka. *Sci Rep* 7, 45940.
388 <https://doi.org/10.1038/srep45940>
389

390 Gibbons, J. D., and S. Chakraborti (2003), *Non-parametric Statistical Inference*, 4th ed., 645 pp., Marcel Dekker, New York
391
392
393 Gregg, P.M., de Silva, S.L., Grosfils, E.B., Parmigiani, J.P. (2012) Catastrophic caldera-forming eruptions:
394 Thermomechanics and implications for eruption triggering and maximum caldera dimensions on Earth, *Journal of*
395 *Volcanology and Geothermal Research*, 241–242, 1–12. <https://doi.org/10.1016/j.jvolgeores.2012.06.009>
396
397 Isaia, R., Vitale, S., Marturano, A., Aiello, G., Barra, D., Ciarcia, S., Iannuzzi, E., & Tramparulo, F. D’A. (2019).
398 High-resolution geological investigations to reconstruct the long-term ground movements in the last 15 kyr at Campi Flegrei
399 caldera (southern Italy). *Journal of Volcanology and Geothermal Research*. Advance online publication.
400 <https://doi.org/10.1016/j.jvolgeores.2019.07.012>
401
402 Marzocchi W, Selva J, Jordan TH (2021), A Unified Probabilistic Framework for Volcanic Hazard and Eruption
403 Forecasting, *Natural Hazards and Earth System Sciences*, 21, 3509–3517. <https://doi.org/10.5194/nhess-21-3509-2021>
404
405 Meletti C, Marzocchi W, D’amico V, Lanzano G, Luzi L, Martinelli F, Pace B, Rovida A, Taroni M, Visini F, Akinci A,
406 Anzidei M, et al. (2021), The new Italian seismic hazard model (MPS19), *Annals of Geophys.*, 64, 1, SE112.
407 <https://doi.org/10.4401/ag-8579>
408
409 Monaco, L., Palladino, D. M., Albert, P. G., Arienzo, I., Conticelli, S., Di Vito, M., Fabbrizio, A., D’Antonio, M., Isaia, R.,
410 Manning, C. J., Nomade, S., Pereira, A., Petrosino, P., Sottili, G., Sulpizio, R., Zanchetta, G., & Giaccio, B. (2022). Linking
411 the Mediterranean MIS 5 tephra markers to Campi Flegrei (southern Italy) 109–92 ka explosive activity and refining the
412 chronology of MIS 5c-d millennial-scale climate variability. *Global and Planetary Change*, 211, Article 103785.
413 <https://doi.org/10.1016/j.gloplacha.2022.103785>
414
415 Natale, J., Ferranti, L., Isaia, R., Marino, C., Sacchi, M., Spiess, V., Steinmann, L., & Vitale, S. (2022). Integrated
416 on-land-offshore stratigraphy of the Campi Flegrei caldera: New insights into the volcano-tectonic evolution in the last
417 15 kyr. *Basin Research*, 34(2), 855–882. <https://doi.org/10.1111/bre.12643>
418
419 Natale, J., Vitale, S., Repola, L., Monti, L., and Isaia, R. (2024); Geomorphic analysis of digital elevation model generated
420 from vintage aerial photographs: A glance at the pre-urbanization morphology of the active Campi Flegrei caldera.
421 *Geomorphology* 460, 109267; <https://doi.org/10.1016/j.geomorph.2024.109267>
422
423 Natale, J., Cascella, E., & Vitale, S. (2025); Tracking the growth and deformation of fissure phreatomagmatic eruptions:
424 Insights from the ca. 3.9 ka Nisida eruption at Campi Flegrei caldera, southern Italy. *GSA Bulletin* 2025.
425 <https://doi.org/10.1130/B38367.1>
426
427 Orsi, G., Di Vito, M. A., & Isaia, R. (2004). Volcanic hazard assessment at the restless Campi Flegrei caldera. *Bulletin of*
428 *Volcanology*, 66, 514–530. <https://doi.org/10.1007/s00445-003-0336-4><https://doi.org/10.1007/s00445-003-0327-4>
429
430 Orsi G, Di Vito MA, Selva J, Marzocchi W (2009) Long-term forecasting of eruption style and size at Campi Flegrei caldera
431 (Italy). *Earth Planet Sci Let* 287:265–276. <https://doi.org/10.1016/j.epsl.2009.08.013>
432
433 Pappalardo, L., Civetta, L., D’Antonio, M., Deino, A. L., Di Vito, M. A., Orsi, G., Caradente, A., De Vita, S., Isaia, R., &
434 Piochi, M. (1999). Chemical and Sr-isotopical evolution of the Phlegraean magmatic system before the Campanian
435 Ignimbrite (37 ka) and the Neapolitan Yellow Tuff (12 ka) eruptions. *Journal of Volcanology and Geothermal Research*,
436 91(1), 141–166. [https://doi.org/10.1016/S0377-0273\(99\)00033-5](https://doi.org/10.1016/S0377-0273(99)00033-5)
437
438 Rivalta, E., Corbi, F., Passarelli, L., Acocella, V., Davis, T., & Di Vito, M. A. (2019). Stress inversions to forecast magma
439 pathways and eruptive vent location. *Science Advances*, 5, eaau9784. <https://doi.org/10.1126/sciadv.aau9784>

440
441 Scarpati, C., Perrotta, A., Lepore, S., & Calvert, A. (2013). Eruptive history of Neapolitan volcanoes: Constraints from
442 $^{40}\text{Ar}/^{39}\text{Ar}$ dating. *Geological Magazine*, 150(3), 412–425. <https://doi.org/10.1017/S0016756812000854>
443
444 Selva, J., Orsi, G., Di Vito, M. A., Marzocchi, W., & Sandri, L. (2012). Probability hazard map for future vent opening at the
445 Campi Flegrei caldera, Italy. *Bulletin of Volcanology*, 74, 497–510. <https://doi.org/10.1007/s00445-011-0528-2>
446
447 Selva J, Costa A, De Natale G, Di Vito MA, Isaia R, Macedonio G (2018), Sensitivity test and ensemble hazard assessment
448 for tephra fallout at Campi Flegrei, Italy, *J Volcanol Geotherm Res* 351, 1-28,
449 <https://doi.org/10.1016/j.jvolgeores.2017.11.024>
450
451
452 SSHAC (Senior Seismic Hazard Analysis Committee) (1997). Recommendations for Probabilistic Seismic Hazard Analysis:
453 Guidance on Uncertainty and Use of Experts, U.S. Nuclear Regulatory Commission, U.S. Dept. of Energy, Electric Power
454 Research Institute, NUREG/CR-6372, UCRL-ID-122160, Vols. 1/2.
455
456 Sparice, D., Pelullo, C., de Vita, S., Arienzo, I., Petrosino, P., Mormone, A., Di Vincenzo, G., Marfè, B., Cariddi, B., De
457 Lucia, M., Vertechì, E., D’Oriano, C., Del Carlo, P., Di Roberto, A., Giaccio, B., Zanchetta, G., & Di Vito, M. A. (2024).
458 The pre-Campi Flegrei caldera (>40 ka) explosive volcanic record in the Neapolitan Volcanic Area: New insights from a
459 scientific drilling north of Naples. *Journal of Volcanology and Geothermal Research*.
460 <https://doi.org/10.1016/j.jvolgeores.2024.108209>
461
462 Tarquini, S., Isola, I., Favalli, M., Battistini, A., & Dotta, G. (2023). TINITALY, a digital elevation model of Italy with a
463 10 m cell size (Version 1.1) [Data set]. Istituto Nazionale di Geofisica e Vulcanologia (INGV).
464 <https://doi.org/10.13127/tinitaly/1.1>

465 Vitale, S., & Natale, J. (2023). Combined volcano-tectonic processes for the drowning of the Roman western coastal
466 settlements at Campi Flegrei (southern Italy). *Earth, Planets and Space*, 75, 38. <https://doi.org/10.1186/s40623-023-01795-7>